Research Square

Preprints are preliminary reports that have not undergone peer review.
They should not be considered conclusive, used to inform clinical practice,
or referenced by the media as validated information.

Directed evolution of a genetically encoded photocatalyst for temporally resolved proximity labeling of subcellular RNAs and proteins

Peng Zou

zoupeng@pku.edu.cn

Peking University https://orcid.org/0000-0002-9798-5242

Yuxin Fang

Peking University

Ziqi Ren

Peking University

Fu Zheng

Peking University

Ruixiang Wang

Peking University

Songrui Zhao

Peking University

Wentao Wang

Peking University

Chen Li

Peking University

Luorong Liu-Yang

Peking University

Chang Lin

Peking University

Article

Keywords:

Posted Date: July 8th, 2025

DOI: https://doi.org/10.21203/rs.3.rs-6890342/v1

License: This work is licensed under a Creative Commons Attribution 4.0 International License.
Read Full License

Additional Declarations: There is **NO** Competing Interest.

Version of Record: A version of this preprint was published at Nature Chemical Biology on September 7th, 2026. See the published version at https://doi.org/10.1038/s41589-026-02313-y.

Directed evolution of a genetically encoded photocatalyst for temporally resolved proximity labeling of subcellular RNAs and proteins

Yuxin Fang[1,#], Ziqi Ren[1,#], Fu Zheng[1,#], Ruixiang Wang[2,#], Songrui Zhao[2], Wentao Wang[1], Chen Li[2], Luorong Liu-Yang[1], Chang Lin[1], Peng Zou[1,2,3,*]

1 College of Chemistry and Molecular Engineering, Synthetic and Functional Biomolecules Center, Beijing National Laboratory for Molecular Sciences, Key Laboratory of Bioorganic Chemistry and Molecular Engineering of Ministry of Education, PKU-IDG/McGovern Institute for Brain Research, Peking University, Beijing, 100871, China

2 Academy for Advanced Interdisciplinary Studies, Peking-Tsinghua Center for Life Sciences, Peking University, Beijing, 100871, China

3 Beijing Advanced Center of RNA Biology (BEACON), Peking University, Beijing, 100871, China

4 Chinese Institute for Brain Research (CIBR), Beijing 102206, China

# These authors contributed equally to this work

* Correspondence: zoupeng@pku.edu.cn

Abstract

In eukaryotic cells, the precise spatial localization of RNAs and proteins is essential for proper cellular function. Genetically encoded photocatalytic proximity labeling techniques have expanded our ability to map subcellular proteomes and transcriptomes, but their temporal resolution remains limited. Here, we introduce Lantern, an engineered flavoprotein optimized via directed evolution, which enables sub-minute, spatially resolved labeling of cellular biomolecules. Lantern is targetable to diverse subcellular compartments, including the endoplasmic reticulum, mitochondria, and stress granules (SGs), to map local transcriptomes (CAP-seq) and proteomes (CAP-MS). Using Lantern, we observed that m^{6}A-enriched RNAs are recruited to SGs within five minutes of stress induction, while ER-proximal RNAs associate with the SG scaffold protein G3BP1 during early SG assembly. Additionally, Lantern was adapted for cell-surface tagging (CAP-CELL), enabling spatially resolved cell typing and the analysis of cell-cell interactions. Collectively, this study establishes Lantern as a powerful tool that offers unprecedented temporal resolution for investigating the dynamic organization of subcellular molecular networks.

Introduction

Eukaryotic cells are intricately compartmentalized to ensure that RNAs and proteins are precisely localized for their specific functions. Rapid repositioning of these molecules is critical for processes such as signal transduction[1], viral infection[2], and cell cycle regulation[3]. For instance, during stress, cells concentrate specific RNAs and proteins into micrometer-sized, membraneless organelles known as stress granules (SGs), which form through distinct assembly stages[4]. Mapping the temporal sequence of molecular recruitment is essential for a complete understanding of cellular stress response mechanisms and SG functionality.

Recent advances in proximity labeling (PL) techniques have transformed the *in situ* mapping of subcellular proteomes and transcriptomes. Engineered biotin ligases (e.g. BioID[5] and TurboID[6]) produce a biotinyl-5′-AMP intermediate that covalently modifies nucleophilic residues (e.g., lysine) on nearby proteins in live cells[5], tissues[6], and animals[6]. However, this method is inefficient for RNA labeling and suffers from limited temporal control due to the presence of endogenous biotin. Engineered peroxidases (e.g. APEX2[7-9] and HRP[10]) address some of these challenges by catalyzing the H_2O_2-dependent oxidation of biotin-phenol, generating highly reactive phenoxyl free radicals that rapidly label both proteins and RNAs within tens of nanometers of the enzyme. Despite their fast kinetics, the high H_2O_2 concentrations required can disrupt redox homeostasis[11]. In contrast, photocatalytic reactions offer superior temporal control and reduced cytotoxicity[12]. For example, μMap employs a blue light-activated iridium complex to generate reactive carbenes for labeling[13]. However, the requirement for an exogenous photocatalyst may result in non-specific background labeling due to small-molecule adsorption. Genetically encoded photocatalysis, in principle, could overcome these challenges by offering precise temporal control while minimizing background interference.

In our previous work, we introduced a genetically encoded photocatalytic PL approach leverages miniSOG[14-16], an engineered flavoprotein derived from the LOV2 (light, oxygen and voltage) domain of *Arabidopsis thaliana* phototropin 2[17]. Upon blue light exposure, miniSOG generates reactive oxygen species (ROS) that oxidize nearby RNAs and proteins, enabling their capture with the nucleophilic probes such as propargylamine (PA) and 3-ethynylaniline (3-EA). This method, termed CAP-seq[14] for RNA labeling and RinID[16]/PDPL[18] for protein labeling, has achieved high spatial specificity across various subcellular compartments, including mitochondria, the endoplasmic reticulum (ER), and SGs[19]. However, the requirement for prolonged blue light exposure (30 mW/cm^2 for 15 min) limits miniSOG's ability to capture rapid processes such as SG assembly. More recently, LITag was developed from a rationally designed miniSOG variant called LOV* (SOPP), which has enabled proteomic profiling with only 1 s of illumination, albeit at a much

higher light intensity (450 mW/cm^2)[20]. Furthermore, the efficiency and spatial specificity of LITag-mediated RNA labeling have yet not been thoroughly examined at the transcriptome level.

In this study, we describe the engineering of a novel miniSOG variant, Lantern (light-activated flavin-binding protein with enhanced proximity labeling activity), via directed evolution. Lantern achieves spatially resolved labeling of both RNAs and proteins in live cells with sub-minute temporal resolution. We demonstrate Lantern's broad utility in mapping subcellular transcriptomes (CAP-seq), proteomes (CAP-MS), and cellular spatial organization (CAP-CELL). Kinetically resolved transcriptomic analyses reveal that m^{6}A-rich RNAs are rapidly recruited into SGs within 5 min of stress onset, and we identify hundreds of ER-proximal RNAs associating with G3BP1 during early SG assembly (10 min post-stress), suggesting a role for the ER membrane in SG biogenesis. Proteomic profiling further shows extensive remodeling of the G3BP1 interactome within the first 30 min of stress, including the time-dependent recruitment of m^{6}A reader proteins. Together, our integrated transcriptomic and proteomic analyses support a model in which RNA mobilization precedes protein recruitment during SG assembly.

Results

Engineering Lantern via mammalian cell-based directed evolution

Directed evolution offers a powerful means to enhance protein function. As a protein-based photocatalyst, miniSOG is especially amenable to such optimization, as its catalytic efficiency could be improved through iterative mutagenesis and selection. A key element in the design of directed evolution scheme is to link the phenotype (i.e. improved catalytic efficiency, protein folding stability, etc.) with the genotype (i.e. protein or gene sequences). However, a challenge of evolving miniSOG lies in correlating intracellular protein/RNA labeling with a selectable phenotype.

Inspired by the MS2–MCP interaction system used in live-cell RNA imaging[21], we developed a directed evolution platform in which a library of miniSOG mutants was fused to a tandem dimer of the MS2 coat protein (tdMCP). By integrating a 24× MS2 array into the 3′ untranslated region (UTR) of target transcripts, we enabled self-directed, light-dependent labeling (Figure 1A). To minimize expression variability, we employed an engineered human embryonic kidney 293T (HEK293T) cell line with a single pre-installed attP site (landing pad)[22]. Transfection with gene sequences flanked by attB sites, followed by recombinase (Bxb1)–mediated integration, ensured stable, single-copy expression of each miniSOG variant[23]. After labeling, RNAs were extracted, biotinylated via click chemistry, enriched on streptavidin beads, and sequenced to quantify labeling efficiency.

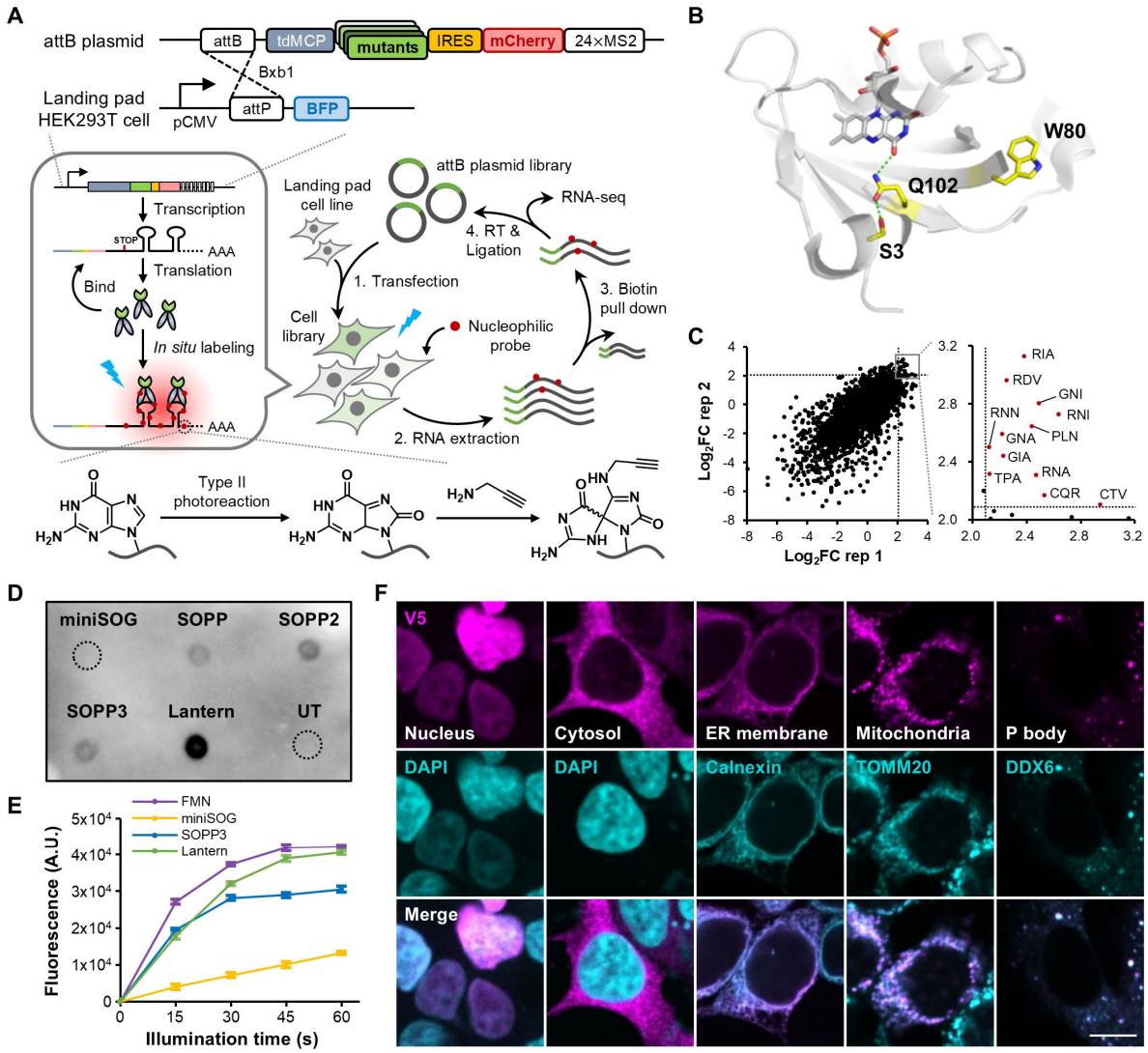


Figure 1. Directed evolution of Lantern. (A) Schematic of the selection procedure. Each variant was targeted to its own transcript via the MCP-MS2 system and catalyzed an RNA labeling reaction with PA on blue-light irradiation. Then the RNAs were clicked with biotin handles, enriched with streptavidin-coated beads and sequenced for activity evaluation. **(B)** The structure of FMN-bound miniSOG with the mutation sites highlighted in yellow. PDB: 6GPU. **(C)** Enrichment fold of all mutants in the replicated second-round selection. Twelve top enriched mutants were shown in the zoom-in figure. **(D)** Representative streptavidin dot blot analysis of RNA labeling catalyzed by different miniSOG variants. UT, untransfected cells. **(E)** The SOSG oxidation curve upon blue-light irradiation. **(F)** Representative immunofluorescence images of HEK293T cells expressing Lantern targeted to different subcellular localizations. Scale bar is 10 μm.

We first validated the system by comparing miniSOG to a photocatalytically inactive mutant, miniSOG^{G39C}[24]. Successful integration of tdMCP-miniSOG or tdMCP-miniSOG^{G39C} was confirmed by the loss of blue fluorescent protein (BFP) signal (Figure S1A) and genomic sequencing (Figure S1B-C). As expected, the G39C mutation reduced labeling efficiency, evident from the lower recovery of miniSOG^{G39C} sequences (Figure S1B). When cells expressing miniSOG and miniSOG^{G39C} were mixed at a 1:100 ratio, miniSOG was enriched 15-fold over the mutant, demonstrating the robustness of our selection system (Figure S1D-E).

In the directed evolution phase, we targeted miniSOG residues S3, W80, and Q102 using site-saturation mutagenesis (Figure 1B). The Q102 residue forms a hydrogen bond with the FMN ring, potentially hindering singlet oxygen ($^1O_2$) production by facilitating electron transfer from the protein to triplet FMN[25]. The S3 residue, which substituted the N3 residue in the original LOV2 domain, interacts with Q102 and may indirectly affect the FMN hydrogen-bond network[26]. Meanwhile, the electron-rich W80 residue is hypothesized to quench triplet FMN[27]. Under blue light selection pressures of 1, 5, or 15 min, our library favored glycine at S3 and alanine, arginine, or asparagine at Q102 while avoiding tryptophan at both positions (Figure S1F-G and Table S1).

In the subsequent round of evolution, we maintained the high selection pressure of 1-min irradiation. We identified 12 mutants surpassing a Log_2 fold-change (Log_2FC) cutoff of 2.1 (Figure 1C and Table S1). Individual testing in the mitochondrial matrix of HEK293T cells (using PA and 1-min blue light exposure) via RNA dot blot revealed that 9 of these outperformed wild-type miniSOG, with the triple mutant S3G/W80N/Q102A showing an 11.6-fold enhancement in labeling (Figure 1D and Figure S1H-I). This mutant was designated as Lantern and used for all subsequent experiments. In terms of RNA labeling efficiency, Lantern outperformed SOPP2 and SOPP3[27] by 3.9- and 3.2-fold, respectively (Figure 1D).

We next characterized the photophysical properties and mammalian cell expression of Lantern. Its absorption and fluorescence spectra are similar to SOPP3 but blue-shifted by 8 nm relative to miniSOG, with an absorption peak at 440 nm (Figure S1J). Using Singlet Oxygen Sensor Green[28], we measured Lantern's $^1O_2$ quantum yield as 0.42, compared to 0.36 for SOPP3 and 0.10 for miniSOG (Figure 1E and Figure S1K). Importantly, Lantern exhibited greater photostability than SOPP3 (Figure S1K). We expressed Lantern in various subcellular compartments, including the nucleus, cytosol, ER membrane, mitochondrial matrix, and processing bodies (P-bodies). Confocal fluorescence microscopy revealed the co-localization of Lantern with the corresponding organelle markers (Figure 1F).

Finally, we evaluated the protein labeling efficiency of Lantern. When expressed in the mitochondrial matrix of HEK293T cells, Lantern exhibited stronger labeling than miniSOG and

SOPP2/3 under 1-min irradiation at 30 mW/cm^2 with 10 mM PA (Figure S1L-M). We then compared Lantern to LITag under intense illumination (1 s at 450 mW/cm^2) in the presence of 1 mM 3-EA. Lantern demonstrated substantially stronger labeling than LITag, a difference that became even more pronounced under lower illumination intensity (30 mW/cm^2 for 1 min), where LITag showed minimal labeling relative to background (Figure S1N). Collectively, the above characterizations establish Lantern as an efficient, genetically encoded photocatalyst for mammalian cells.

Characterizing the spatial specificity and sensitivity of Lantern-mediated proximity labeling

To assess Lantern's spatial specificity and sensitivity, we targeted it to the ER membrane and benchmarked its performance against established methods such as APEX-seq[29] and miniSOG-based CAP-seq[14] (Figure 2A). The ER membrane is known to be enriched with mRNAs encoding secretory proteins[30]. We generated a HEK293T cell line stably expressing ER membrane-targeted Lantern by fusing it to the N-terminus of the ER translocon subunit Sec61β (ERM-Lantern)[31]. Cells were labeled with 10 mM PA under blue light irradiation for durations ranging from 1 to 15 min. RNA dot blot analysis showed that biotinylation signals increased with irradiation time, with Lantern displaying significantly higher labeling efficiency than miniSOG (Figure S2A). Notably, 1 min of Lantern labeling produced an equivalent signal to 15 min of miniSOG labeling (Figure S2A).

RT-qPCR analysis revealed that secretory genes such as *SSR2* and *TMX1* were enriched approximately 1,000-fold with ERM-Lantern compared to no-light controls. Moreover, 1 min of Lantern labeling yielded 2.2- and 2.0-fold higher enrichment of *SSR2* and *TMX1*, respectively, relative to 15 min of miniSOG labeling (Figure S2B). Although enrichment levels for secretory genes remained consistent between 1- to 15-min light exposures, prolonged irradiation increased background (i.e. non-secretory gene) enrichment by approximately 4-fold (Figure S2B). Confocal imaging further confirmed that, after 1 min of irradiation, biotinylation signals from ERM-Lantern co-localized precisely with Lantern expression and the endogenous ER marker calnexin. Biotinylation signal was minimal in negative controls omitting light or Lantern expression, or when ERM-miniSOG was used as the photocatalyst (Figure 2B).

Additionally, we also compared RNA labeling results of Lantern-mediated CAP-seq with those of APEX-seq. An APEX labeling experiment was conducted as previously reported[29] using an APEX2-Sec61β stable cell line. The biotinylated RNAs were enriched with streptavidin-coated beads and analyzed by dot blot and RT-qPCR (Figure 2C-D). Using the same 1-min labeling time window, Lantern-mediated CAP-seq exhibited much stronger biotinylation signals than APEX-seq

or miniSOG-mediated CAP-seq (Figure 2C). In RT-qPCR analysis, Lantern enriched the secretory genes *SSR2* and *TMX1* with 119- and 150-fold higher yield than APEX-seq. On the contrary, the yields for non-secretory genes, *FAU* and *MTCO2*, were only 30- and 26-fold higher with Lantern-mediated CAP-seq than with APEX-seq (Figure 2D and Figure S2C-D). Given the successful applications of APEX-seq across various subcellular localizations, we reason that the significantly stronger labeling achieved with Lantern-mediated CAP-seq enables studies involving small amounts of materials, such as neuronal samples.

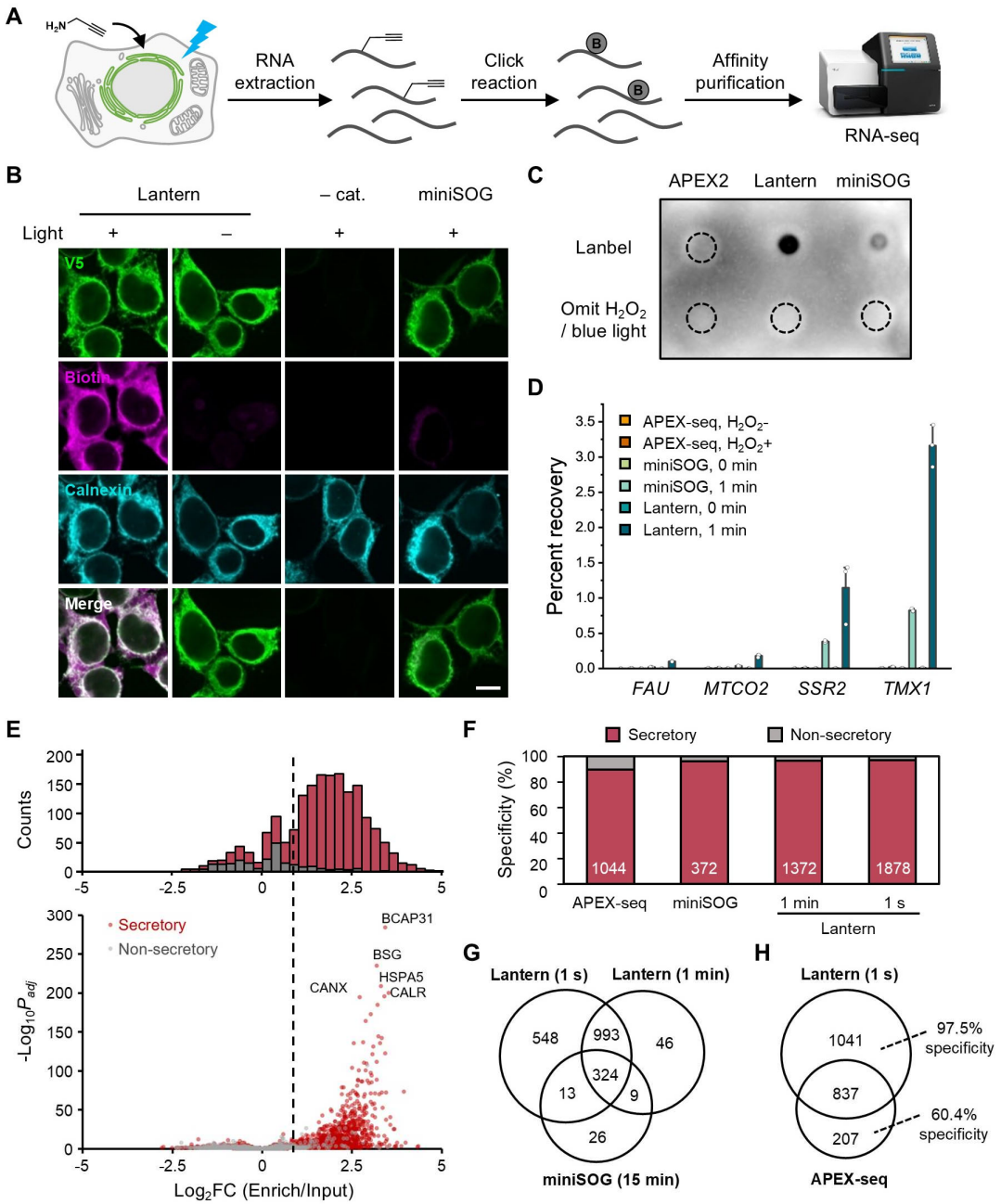


Figure 2. Profiling the ERM transcriptome with Lantern-mediated CAP-seq. (A) Schematic of the CAP-seq workflow. Lantern was targeted to the ER membrane via fusion with Sec61β. ERM-proximal RNAs were labeled with 10 mM PA during 1 min of irradiation. Following a click reaction to install biotin handles, the labeled RNAs were enriched with streptavidin-coated beads and sequenced. **(B)** Representative immunofluorescence images of HEK293T cells labeled with ERM-Lantern. Scale bar: 10 μm. **(C-D)** Dot blot **(C)** and RT-qPCR **(D)** analyses comparing the labeling results of APEX-seq and CAP-seq. Cells stably expressing APEX-Sec61β were labeled with 0.5 mM BP and 1 mM H_2O_2 for 1 min. Cells stably expressing miniSOG-Sec61β or Lantern-Sec61β were labeled with 10 mM PA and 1 min irradiation of blue light at 30 mW/cm^2. *SSR2* and *TMX1* are secretory transcripts. *FAU* is a transcript that encodes a cytosol-localized protein. *MTCO2* belongs to the mitochondrial transcriptome. The percent recovery of each gene was calculated based on the relative RNA abundance before and after enrichment. Each qPCR reaction was conducted in triplicates. **(E)** Volcano plot of the ERM-Lantern dataset. Red and grey dots represent secretory and non-secretory mRNAs, respectively. Vertical dashed line indicates the cutoff of 0.925. Upper panel: histogram showing the distribution of secretory (red) and non-secretory mRNAs (grey). **(F)** Comparison of the spatial specificity of Lantern-mediated CAP-seq with other RNA proximity labeling techniques. The number of transcripts captured by each method is indicated in the columns. **(G-H)** Venn diagrams comparing the CAP-seq datasets obtained from Lantern and miniSOG **(G)**, and comparing Lantern CAP-seq with APEX-seq, with the spatial specificity of each method indicated on the side **(H)**.

To quantitatively measure the spatial specificity and sensitivity of Lantern-mediated RNA labeling in live cells, we performed duplicated CAP-seq experiments on ERM-Lantern cells under 1-min blue light irradiation at 30 mW/cm^2 in the presence of 10 mM PA. Extracted RNAs were biotinylated via click chemistry, affinity-purified on streptavidin beads, and then sequenced. Differential expression analysis (DESeq2) comparing 'Enrich' versus 'Input' samples identified 1,382 ER membrane-proximal (ERM) RNAs, including 1,372 mRNAs and 10 non-coding RNAs (Figure 2E, Figure S2E and Table S2). Annotation using Gene Ontology Cellular Component and Human Protein Atlas databases revealed that 96.4% (1,323/1,372) of these mRNAs are linked to the secretory pathway. In comparison, APEX-seq enriched 1044 mRNAs with 89.7% specificity[29]. While Lantern and miniSOG[14] exhibit comparable spatial specificity (96.4% vs. 96.2%), Lantern demonstrated markedly higher sensitivity by identifying 1, 372 mRNAs versus 372 with miniSOG, despite the shorter irradiation time (1 min vs. 15 min) (Figure 2F).

Encouraged by these results, we further tested a 1-s RNA labeling protocol by increasing the blue light intensity from 30 to 450 mW/cm^2. RT-qPCR confirmed effective enrichment of *SSR2* and *TMX1* after just 1 s of irradiation, with recovery rates comparable to those observed after 1 min at 30 mW/cm^2 (Figure S2F). This 1-s approach reduced the total light dosage by a factor of four. Next-generation sequencing (NGS) of the 1-s samples identified 1,878 mRNAs with 97.3%

secretome specificity (Figure 2F and Table S2). The strong overlap between the 1-min and 1-s datasets underscores Lantern's robustness. Together, these datasets covered 93% (324/372) of the ERM-miniSOG dataset (Figure 2G). Notably, 837 mRNAs were common to both the 1-s Lantern and APEX datasets, representing 44.6% of the Lantern data and 80.2% of APEX-seq (Figure 2H). Overall, these results highlight Lantern-mediated CAP-seq as a powerful tool for achieving exceptional spatial specificity and sensitivity.

Mapping stress granule transcriptome during stress-induced assembly

After validating Lantern's spatial precision and sensitivity, we applied Lantern-mediated CAP-seq to map the transcriptome associated with SGs during assembly. SG formation is a multistage process that begins with the assembly of stable "core" components, which then recruit more dynamic "shell" components to form mature SGs. In response to sodium arsenite ($NaAsO_2$) treatment, visible SG condensates emerge around 13 min post-stress and continue to grow until approximately 40 min[4].

Previous studies have mapped dynamic changes in the SG-proximal transcriptome during heat shock using APEX-seq with the initiation factor eIF4A1 as a bait protein[32]. However, the kinetics of RNA recruitment to SGs under other stress conditions remain unclear. Similarly, while miniSOG-mediated CAP-seq profiling using the SG core component G3BP1 revealed transcriptome remodeling during oxidative stress, its 15-min labeling requirement limits temporal resolution[19]. Another recent method, based on reverse transcription of RBP binding sites, achieved mapping G3BP1-interacting transcripts during arsenite-induced SG assembly but relied on a 10-min paraformaldehyde fixation period, which is incompatible with the rapid dynamics of SG assembly[33]. By leveraging Lantern's rapid labeling capability, we aimed to monitor SG transcriptome dynamics in real time, enabling a more precise capture of the transient events during SG assembly.

We generated a HEK293T cell line stably expressing Lantern fused to the SG scaffold protein G3BP1 (G3BP1-Lantern) through lentiviral transduction. To control for RNAs interacting with diffusive G3BP1 outside of SGs, we also constructed a cell line expressing Lantern fused to a nuclear export signal (Lantern-NES). Western blot analysis confirmed that G3BP1-Lantern expression was approximately 85% of endogenous G3BP1 levels (Figure S3A-B). Both eIF2α phosphorylation assays and SG size quantification validated that SG assembly dynamics in G3BP1-Lantern cells were consistent with previously published data (Figure S3C-D). To optimize labeling conditions, we treated cells with 0.5 mM $NaAsO_2$ to induce stress and tested irradiation times ranging from 10 to 60 s at 30 mW/cm^2, in the presence of 10 mM PA. RT-qPCR

demonstrated progressive enrichment of G3BP1-associated genes *DYNC1H1* and *NORAD* with longer irradiation times (Figure S3E). We eventually chose 30 s to balance efficiency and temporal resolution.

We performed duplicated CAP-seq labeling experiments at six time points: 0, 5, 10, 15, 30, and 60 min post-stress induction, using Lantern-NES as a control (Figure 3A). Immunofluorescence confirmed that G3BP1-Lantern assembly kinetics aligned with known SG dynamics following treatment with 0.5 mM $NaAsO_2$ (Figure 3B). Correlation analysis revealed highly reproducible RNA enrichment by G3BP1-Lantern, with Pearson's correlation coefficients exceeding 0.95 for FPKM values in replicate measurements at each time point (Figure S3F). We employed DESeq2 to assess RNA enrichment using two approaches: 1) comparing RNAs enriched from G3BP1-Lantern versus Lantern-NES cell lines (G3BP1 vs. Untargeted), and 2) comparing RNAs post- versus pre-enrichment from the G3BP1-Lantern cell line (Enrich vs. Input). Genes consistently detected by both methods, passing a cutoff of $Log_2FC > 0.3$ and $P_{adj} < 0.05$, were defined as G3BP1-proximal RNAs. Our analysis identified 1,714, 1,558, 2,606, 2,511, 2,237, and 1,815 transcripts at t = 0, 5, 10, 15, 30, and 60 min, respectively (Table S3). Among these, 876 transcripts were consistently enriched at all six time points, accounting for 26.6% of the total 3289 transcripts enriched at least once (Figure S3G). Cross-correlation analysis of Log_2FC (G3BP1 vs. Untargeted) values across time points revealed a gradual decrease in Pearson's r values over time, indicating high temporal resolution in our datasets (Figure S3H).

We compared the Lantern CAP-seq dataset obtained at t = 60 min with the one previously obtained with miniSOG[19]. Notably, 85.3% of transcripts identified by miniSOG-mediated CAP-seq overlapped with those detected by Lantern-mediated CAP-seq, similar to the overlap observed with the ER-membrane transcriptomes. Lantern-mediated CAP-seq also identified 1,425 new transcripts, none of which were present in the previously defined SG-excluded list (Figure S3I). We also compared our dataset with SG transcriptome obtained from biochemical purification. We found that 700 out of 1,815 transcripts (38.6%) in our 60-min dataset overlapped with those identified by SG isolation, representing 43.1% of that dataset (Figure S3J).

To validate our profiling, we performed single-molecule fluorescence *in situ* hybridization (smFISH) to detect the localization of RNAs enriched in our SG dataset, specifically *SPTAN1* ($Log_2FC = 2.03$) and *HSP90B1* ($Log_2FC = 1.18$) (Figure 3C). Confocal microscopy revealed that these mRNAs formed visible clusters co-localizing with SGs after 60 min of $NaAsO_2$ treatment (Figure 3D). In contrast, the smFISH signals for *INTS1*, a transcript not enriched in stressed cells ($Log_2FC = 0.57$, $P_{adj} = 0.71$), were mostly excluded from SGs (Figure 3D).

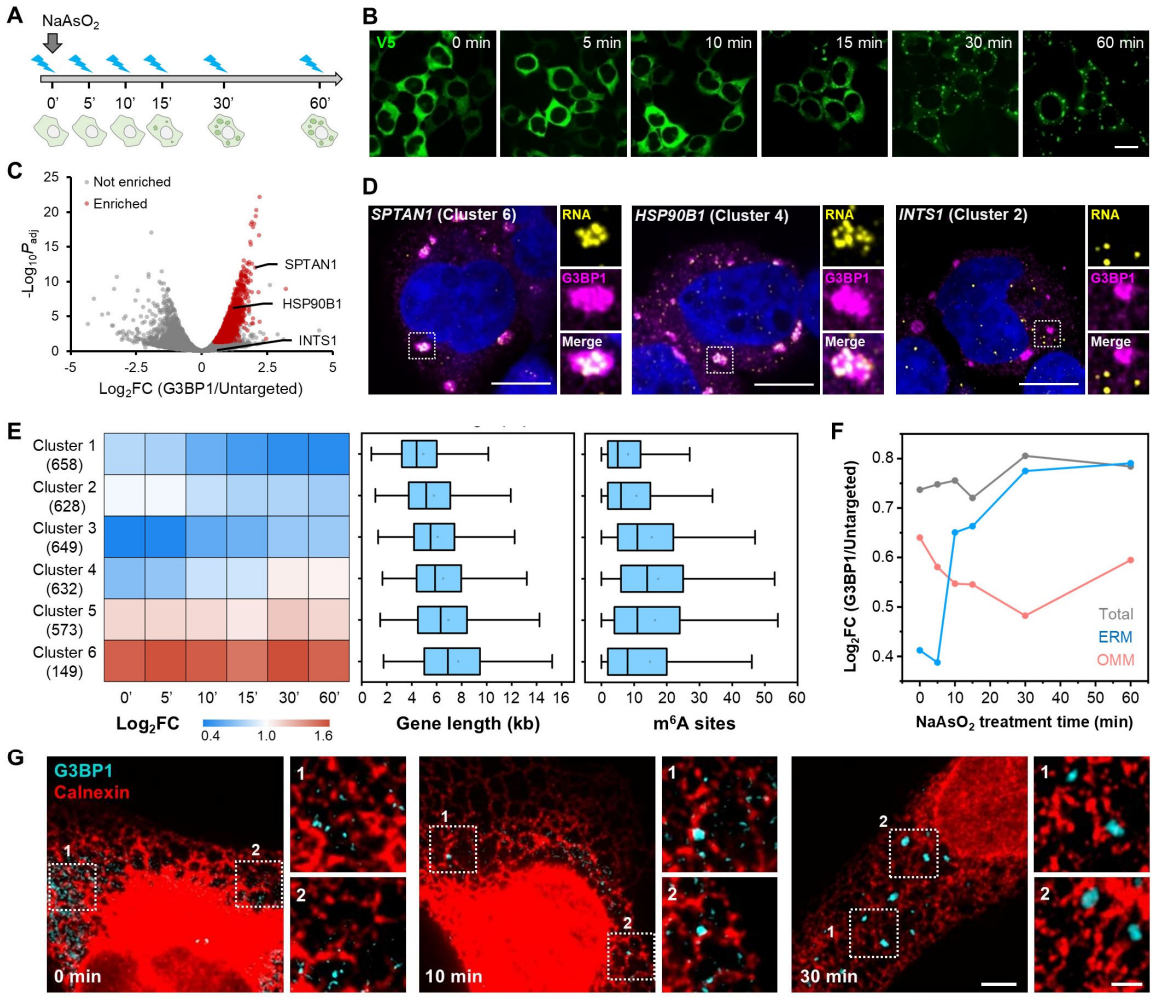


Figure 3. Tracking the dynamic G3BP1-interacting transcriptome during SG assembly. (A) Schematic of temporally resolved SG transcriptome profiling. **(B)** Immunofluorescence images of HEK293T cells expressing G3BP1-Lantern after treatment with 0.5 mM $NaAsO_2$ for 0-60 min. Scale bar: 20 μm. **(C)** Volcano plot showing the enrichment of SG RNAs at 60 min post-stress. **(D)** Representative smFISH images of enriched SG transcripts *SPTAN1* and *HSP90B1*, and non-enriched transcript *INTS1*. Scale bar: 10 μm. **(E)** RNAs identified by CAP-seq are categorized into 6 clusters depending on their enrichment time course (left). Middle: box plot comparing the gene lengths. Right: box plot comparing the number of m^6A sites. The box marks the first and third quartiles; whiskers indicate the minima and maxima; the central line represents the median; outliers beyond 1.5x inter-quartile range were excluded. Gene length and m^6A information were referenced from Ensembl website and from C. Liu *et al.,* 2022, *Nat Biotechnol*. **(F)** Average Log_2FC values of ERM RNAs (blue), OMM RNAs (pink), and total RNAs (grey) during the SG assembly. **(G)** Representative immunofluorescence images of U-2 OS treated with 0.5 mM $NaAsO_2$ for 0-30 min. G3BP1 and calnexin (ER tubule marker) are visualized with antibody staining. Zoom-in views of boxed regions are shown on the right. Scale bars: 20 μm (full images) and 2 μm (zoom-in).

To further investigate SG transcriptome dynamics, we employed *k*-means clustering to categorize the 3,289 enriched transcripts into six groups based on their Log_2FC (G3BP1 vs. Untargeted) values (Figure 3E). Clusters 1 and 2, characterized by short transcript lengths and low N^6-methyladenosine (m^6A) levels, were identified as stress-sensitive interactors that dissociated from G3BP1 in response to stress. In contrast, clusters 3 and 4 comprised 1,281 RNAs that associate more with G3BP1 upon oxidative stress. Compared to stress-sensitive interactors (i.e. clusters 1 and 2), these stress-dependent interactors (i.e. clusters 3 and 4) have, on average, 1.74-fold higher m^6A levels and 1.18-fold longer gene lengths, resulting in overall 1.47-fold higher m^6A density (Figure 3E). Clusters 5 and 6 contained 722 stress-independent interactors that remain associated with G3BP1 under both basal and stressed conditions. These RNAs likely belong to a stable network involving SG core components and are notably longer, particularly in coding sequences (CDS), averaging 1.69-fold longer than other RNAs (Figure S3K-M).

Notably, mRNAs *HSP90B1* and *CANX* were highly enriched in both our ERM and SG CAP-seq datasets. Their localizations in stressed cells were validated by smFISH (Figure 3D and Figure S3N), prompting us to investigate potential cross-talk between SG and ER membrane. For RNAs in our ERM-Lantern dataset, their Log_2FC (G3BP1 vs. Untargeted) increased dramatically at 10-min post-stress onset (Figure 3F). This kinetics is even faster than the increase of granule size (Figure S3D). To rule out the possibility that the Log_2FC (G3BP1 vs. Untargeted) values for cellular RNAs are overall increasing, we repeated the analysis for total RNAs, confirming that their changes remained minimal (Figure 3F).

To examine whether the observed trend is specific for ERM RNAs, we performed CAP-seq at another subcellular location. We chose the outer mitochondrial membrane (OMM) as the target and expressed Lantern at the OMM through fusion with the C-terminal 31 amino acids of mitochondrial antiviral-signaling (MAVS) protein (OMM-Lantern). CAP-seq analysis with OMM-Lantern identified 1,490 enriched transcripts, including 1,294 mRNA, 186 pseudogenes, 6 lncRNA, 3 antisense RNA and 1 miscRNA (Table S4). Among these, 70 (4.7%) were enriched by G3BP1-Lantern at 60 min post-stress. In contrast to ERM RNAs, the Log_2FC (G3BP1 vs. Untargeted) values of these OMM-proximal RNAs gradually decreased during the first 30 min post-stress (Figure 3F). We further applied our analysis to RNA datasets obtained from APEX-seq atlas. Whereas cytosolic RNAs were the most enriched across all time points, ERM RNAs exhibited a significant increase in enrichment post-stress (Figure S3O). No significant enrichment was observed for RNAs from other subcellular localizations (Figure S3O).

The above data implicate a role of ER membrane in SG assembly. To investigate this, we performed immunofluorescence in U-2 osteosarcoma (U-2 OS) cells to examine the co-localization of G3BP1 and the ER during early SG assembly. At 10 min post-stress, we observed small G3BP1 clusters associated with ER tubules (Figure 3G). As SGs continued to grow, they became less associated with the ER at 30 min post-stress. These imaging results suggest that interactions between G3BP1 and the ER strengthen during early SG assembly, indicating that at least a subset of SGs forms directly on the ER surface.

Profiling stress granule proteome during assembly with CAP-MS

To corroborate our transcriptomic analysis, we sought to investigate the proteomic changes of SG components during stress (Figure 4A). In the G3BP1-Lantern HEK293T cell line, we compared Lantern-mediated protein labeling efficiency with 10 mM PA or 1 mM 3-EA probe, both containing the alkyne functional handle. Following 30 s of irradiation at 150 mW/cm^2, cells were lysed, and the lysate containing alkynylated proteins was clicked with biotin-conjugated azide. Streptavidin blot analysis showed that 3-EA yielded higher signal-to-noise ratio than PA (Figure S4A). We thus used 1 mM 3-EA for all subsequent proteomic labeling experiments. In G3BP1-Lantern cells stressed with sodium arsenite for 5 to 60 min, immunofluorescence imaging confirmed the good co-localization between Lantern-mediated protein labeling and the SG marker G3BP2 at various time points, thus demonstrating the method's high spatial specificity of mapping SG assembly (Figure 4B).

For quantitative proteomics (CAP-MS), We designed a TMT-labeling experiment to map G3BP1-proximal proteins at 0, 15, 30, and 60 min post-stress. At each time point, we included a Lantern-NES control to normalize CAP-MS biases, along with omitting-light and omitting-Lantern controls at t = 60 min (Figure 4C). The experiment was conducted in duplicates, and normalized ion intensity ratios were calculated against these controls (Supplemental Methods). The mass spectrometry intensities of replicated experiments are highly correlated (Pearson's coefficients r > 0.8). (Figure S4B). At 60 min post stress, highly enriched proteins included canonical SG components, including G3BP1/2, CAPRIN1, and UBAP2L (Figure 4D). Using a cut-off ratio of 1.1, we identified 87 proteins consistently enriched across replicates as SG components (Table S5). We compared our SG protein list with published RNA granule database. Of the 87 identified proteins, 85 (97.7%) were classified as SG components (Tiers 1-3), and 74 (85.1%) belonged to the gold-standard SG proteome (Tier 1) (Figure 4E). Our dataset showed comparable coverage and strong consistency with previously reported SG proteomes identified by APEX2 and BioID, further validating our labeling approach (Figure 4F).

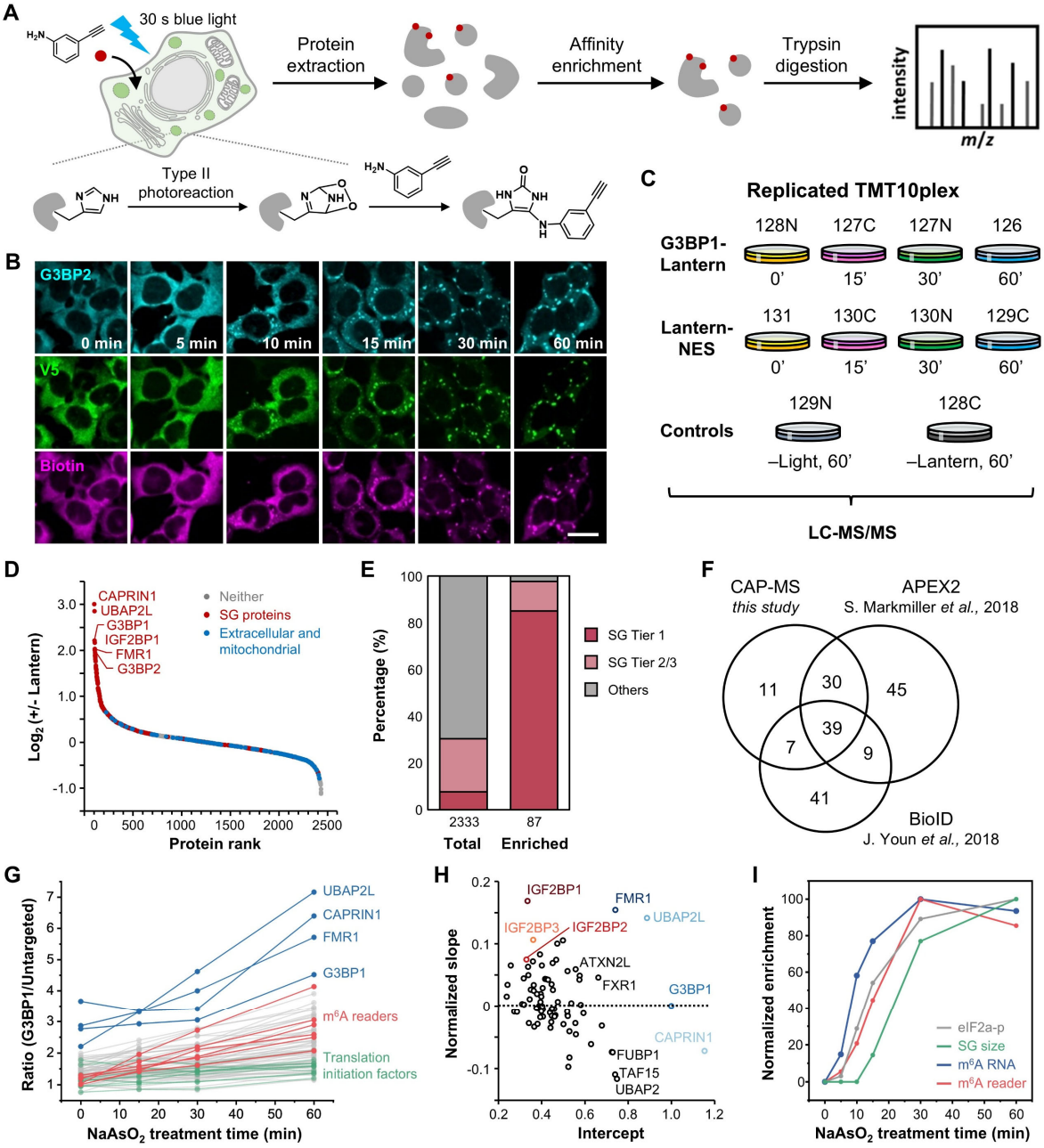


Figure 4. Temporally resolved mapping of SG proteome with CAP-MS during assembly. (A) Schematic of CAP-MS with G3BP1-Lantern in the presence of 1 mM 3-EA. **(B)** Immunofluorescence images of HEK293T cells treated with 0.5 mM $NaAsO_2$ for 0-60 min before CAP-MS labeling. Scale bar: 20 μm. **(C)** Schematic of TMT-based quantitative proteomics to profile G3BP1-interacting proteome at 0-60 min post-stress. **(D)** Protein rank based on +/- Lantern MS intensity ratios. Red: canonical SG proteins. Blue: extracellular or mitochondrial matrix proteins (false positives). **(E)** The SG specificity of the proteins enriched at 60 min post-stress. The SG Tier 1-3 annotations are from the RNA granule database. **(F)** Venn diagram comparing the SG proteome datasets identified by

Lantern-mediated CAP-MS, APEX2 and BioID. **(G)** Time course of CAP-MS enrichment ratio (G3BP1 vs. untargeted) from 0 to 60 min post-stress. **(H)** Plot showing the intercept and normalized slope of enrichment ratio for the 87 SG proteins identified. **(I)** The time course of m^6A RNA (blue) and m^6A binding protein (red) recruitment to G3BP1. Changes in eIF2α phosphorylation (grey) and SG size (green) are shown for comparison.

Among the 87 SG proteins, 84 (96.6%) were known RNA-binding proteins. Additionally, our dataset included 18 P-body proteins, 8 DNA/RNA helicases, 7 canonical m^6A readers, and 5 ubiquitin-related proteins (Table S5). We calculated G3BP1/Untargeted ratios at each time point and plotted their temporal dynamics. Most proteins exhibited an upward trend, with well-characterized SG components (e.g., G3BP1, CAPRIN1, FMR1, UBAP2L) ranking high across all time points, suggesting pre-existing G3BP1-associated protein-protein interaction networks before stress (Figure 4G). In contrast, some SG proteins were enriched in a stress-dependent manner. For instance, IGF2BP1, a cytoplasmic m^6A reader, ranked high at t = 60 min but showed minimal enrichment before stress (Figure 4G). Previous studies have shown that m^6A readers, including YTHDF1-3 and IGF2BP1-3, partition into liquid condensates such as P bodies and SGs along with m^6A-rich mRNAs[34-36]. Knocking down YTHDF1/3 significantly inhibits SG formation, underscoring their critical role in SG assembly[36].

To further characterize the dynamics at early stages of SG assembly, we conducted another TMT-labeling-based quantitative proteome study, focusing on proteins labeled and enriched at 0, 5, 10, and 15 min post-stress (Figure S4C). Sample preparation and data analysis followed the same procedures as described above. We calculated and plotted the G3BP1/Untargeted intensity ratios for 87 SG proteins during the 0-15 min period of stress. Consistent with the results observed during 0-60 min of stimulation, most of the SG proteins, including the bait protein G3BP1, exhibited an increasing trend in their enrichment ratios (Figure S4D). We reasoned that the increased enrichment ratios can be partially caused by enhanced Lantern labeling, as the local concentration of photocatalyst increases alongside SG assembly. To exclude interference from this factor, we normalized the enrichment ratio of each protein with respect to that of G3BP1. The normalized ratio curves indicated that interactions between G3BP1 and m^6A readers began to increase at 10 min post-stress (Figure S4E). To quantitatively describe the dynamics of protein-protein interactions during SG assembly, we conducted linear regression analysis using the normalized ratios over time. We ranked the SG proteins according to the intercepts and slopes of their regression curves, with IGF2BP1 demonstrating the largest slope while a small intercept, indicating a weak interaction with G3BP1 at basal levels but the most significant enhancement in its interaction with G3BP1 upon stress (Figure 4H). Interestingly, G3BP1, CAPRIN1, USP10, and

other highly enriched SG proteins were previously reported to be repelled by m^{6}A RNAs in unstressed cells[37], which can explain the small intercepts but large slopes of most m^{6}A readers in our analysis.

This observation of m^{6}A-binding proteins in our dataset prompted us to further investigate the correlation between m^{6}A levels and RNA recruitment to SGs. We divided the total human RNAs into three categories: high, medium, and low m^{6}A levels, and calculated their enrichment ratios via dividing their normalized counts from the sequencing results of G3BP1-Lantern cells by the normalized counts from the sequencing results of Lantern-NES cells. Among all three classes of RNAs, RNAs with high m^{6}A levels responded the most quickly upon stress and demonstrated the highest G3BP1/Untargeted ratio at 60 min post stress (Figure S4F). To further explore the temporal order of SG resident recruitment, we compared the enrichment curves of m^{6}A RNA (high and medium) and m^{6}A reader proteins, together with the dynamics of eIF2α phosphorylation and SG size growth. Interestingly, the enrichment of m^{6}A RNAs showed the fastest rise in response to stress, reaching ~15% maximum enrichment at t = 5 min and ~58% maximum enrichment at t = 10 min. In comparison, eIF2α phosphorylation showed a maximum increase of ~3% at t = 5 min and ~29% at t = 10 min. The enrichment curve of m^{6}A readers exhibited dynamics similar to the increase curve of eIF2α phosphorylation, and the increase of SG size showed the slowest dynamics (Figure 4I). The lagging of the SG-size curve suggests the accumulation of SG residents around G3BP1 before the occurrence of visible G3BP1 condensates. As two major components of SGs, m^{6}A RNAs appear to be recruited by G3BP1 earlier than m^{6}A reader proteins. This analysis highlights the power of Lantern to spatially resolve the subcellular proteome with sub-minute temporal resolution.

Profiling stress granule transcriptome in primary neuron culture

Building on our successful RNA labeling in HEK293T cells, we extended our investigation to cultured neurons, which is a more complex system due to their cellular diversity and increased vulnerability to cytotoxicity (Figure 5A). Given the association of SGs with neurodegenerative disorders, we used arsenite-challenged cortical neurons to elucidate the composition of neuronal SGs. In our initial experiments, the standard treatment of 0.5 mM $NaAsO_2$ for 1 h, effective in immortalized cell lines, failed to induce SG formation in all neurons. Extending the exposure to 3 h compromised neuronal survival, whereas treating neurons with 0.25 mM $NaAsO_2$ for 3 h successfully induced SG formation in most cells (Figure S5A-B). We next expressed a G3BP1-miniSOG fusion protein in cortical neurons via lentiviral transduction and performed labeling with 15 min of irradiation. However, both immunofluorescence imaging and RNA dot blot analysis

revealed high background signals in wild-type neurons lacking the fusion protein (Figure S5C-D), suggesting that miniSOG was ineffective for RNA labeling in neurons.

Subsequently, we replaced miniSOG with Lantern and optimized the irradiation time. 1 min of blue light exposure produced a strong biotinylation signal in neurons expressing G3BP1-Lantern, with minimal background observed in cells without Lantern (Figure 5B and Figure S5E-F). We thus adopted 1 min as the optimal condition for SG transcriptome profiling in cortical neurons. Primary cultures of rat cortical neurons were transduced with a lentivirus expressing G3BP1-Lantern at 3 days *in vitro* (DIV3), and CAP-seq labeling was performed at DIV8. To capture SG assembly dynamics, samples were collected 3 h after stress induction. In addition to the Input control, we included an omitting-Lantern control (wild type) and a Lantern-NES control (untargeted) to account for non-specific adsorption and labeling signals from diffusing G3BP1-Lantern outside SGs. DESeq2 analysis comparing the Enrich results with the Input, wild-type, and untargeted controls yielded 1268, 1246, and 769 transcripts, respectively, with 321 transcripts commonly enriched across all conditions (Table S6).

For validation, we selected four transcripts (i.e. *Atp5f1a*, *Elp2*, *Wdr6*, and *Tusc3*) that were highly enriched ($Log_2FC > 1$) and two transcripts (*Tet3* and *Ybx1*) that were significantly depleted ($Log_2FC < -1$) at 3 h post-stress for imaging analysis (Figure 5C). Immunofluorescence combined with smFISH revealed that the enriched targets co-localized with SGs, with co-localization ratios ranging from 0.5 to 0.7. In contrast, the depleted targets exhibited markedly lower co-localization ratios (0.24 for *Tet3* and 0.22 for *Ybx1*) (Figure 5C). Although the smFISH signal for *Ybx1* partially overlapped with the SG marker G3BP2, a substantial portion was detected outside SGs, resulting in a lower overall co-localization ratio.

Spatially resolved cellular tagging with Lantern

We investigated whether the robust photocatalytic protein labeling with Lantern could be repurposed for cell typing by tagging cell surface proteins (CAP-CELL). To display Lantern on the cell surface, we fused it with an N-terminal murine Ig *κ*-chain leader sequence and a C-terminal transmembrane domain from platelet-derived growth factor receptor (Lantern-TM). In the presence of biotin-conjugated primary amine probe (Btn-NH_2) and blue light illumination, proteins near Lantern-TM are tagged with biotin. These biotinylated proteins on the cell surface are then stained with streptavidin-conjugated fluorescent dyes, and the labeled cells are isolated by FACS for downstream gene expression analysis (Figure 6A). Immunofluorescence analysis showed strong co-localization between Lantern-TM expression and biotinylation signals (Figure 6B), indicating successful cell surface labeling.

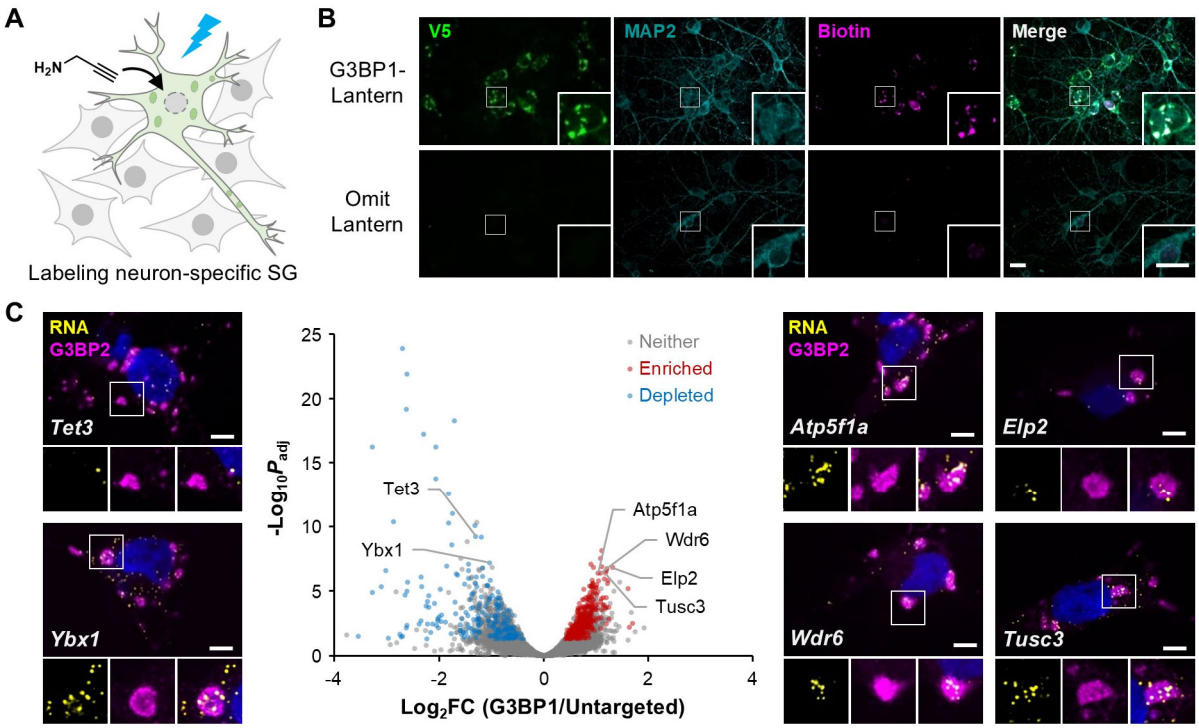


Figure 5. Profiling the SG transcriptome in rat cortical neurons with Lantern-mediated CAP-seq. (A) Schematic of labeling neuron-specific SGs with G3BP1-Lantern. **(B)** Immunofluorescence images showing rat cortical neurons labeled with Lantern at DIV8. Neurons were treated with 0.25 mM $NaAsO_2$ for 3 h. Scale bar: 20 μm. **(C)** Volcano plot (middle) showing the enrichment of SG RNAs in rat cortical neurons. Red and blue dots indicate enriched and depleted RNAs, respectively. Representative smFISH images of SG-enriched transcripts (*Atp5f1a*, *Elp2*, *Wdr6*, and *Tusc3*) are shown on the right, and SG-depleted transcripts (*Tet3* and *Ybx1*) are shown on the left. Scale bar: 5 μm.

The photocatalytic proximity labeling technique enables precise spatial control when combined with a digital micromirror device (DMD)-assisted illumination system. In our study, we co-expressed Lantern-TM with either mCherry (red) or mTurquoise (cyan) fluorescent protein (FP) markers in HEK293T cells. The two cell populations were then mixed to form a co-culture model (Figure 6C). For the mCherry-expressing cells, fluorescence imaging was used to generate a DMD mask that specifically targeted these cells for illumination. In the presence of 2 mM Btn-NH_2, the cells were selectively illuminated with a 445-nm laser through the DMD. After illumination, the cells were dissociated using trypsin, stained with streptavidin-conjugated dyes, sorted by FACS, and subsequently analyzed by RT-qPCR (Figure 6D). We optimized the irradiation time (2 min) (Figure S6A) and performed two independent replicated experiments. The same protocol was then applied to the mTurquoise-expressing cells in two additional replicates (Figure S6B). FACS

analysis demonstrated that over 80% of the sorted cells expressed the expected FP (Figure 6E and Figure S6C), a result corroborated by enriched FP gene signals in the RT-qPCR analysis (Figure 6F).

Encouraged by these results, we applied CAP-CELL to study spatial transcriptomic changes during cancer cell migration. A Mouse Colon 38 (MC38) cancer cell line was engineered to stably express Lantern-TM. Testing various durations of 445-nm irradiation revealed that 1 min was sufficient for robust FACS detection (Figure S6D). To mimic cell migration, cells were initially confined using a culture insert to create a 500-μm cell-free gap. After 24 h of migration post-insert removal, CAP-CELL labeling was performed with the DMD system. Two spatial groups were defined: “Near” cells within a ~200-μm band at the wound edge, and “Far” cells at least 300 μm away (Figure 6G). For each group, 50 cells with high biotin signals were isolated for RNA sequencing in five replicates. Differential expression analysis revealed that “Near” cells were enriched in genes associated with migration and adhesion (e.g., *Actb*, *Fbln2* and *Tubb5*) (Figure 6H) and exhibited upregulation of cancer-related signaling genes such as *Snap25*, *Spry2* and *Ppp3ca* (Table S7). Gene ontology analysis further highlighted translation regulation, ribosome biogenesis, and cell adhesion as active pathways in migrating cells (Figure S6E).

During CAP-CELL optimization, we observed that prolonged illumination increased biotinylation in untransfected cells, suggesting inter-cell labeling possibly due to ROS diffusion (Figure S6A and Figure S6D). We thus hypothesized that tuning the irradiation conditions might enable CAP-CELL to map contact-dependent cell-cell interactions. To test this, we modeled CD40/CD40L interactions by separately transfecting HEK293T cells with CD40L-Lantern (bait) and CD40 (prey). After mixing, cells were incubated with 100 μM Btn-NH_2 and exposed to blue light (30 mW/cm^2) for up to 15 min. Untransfected cells served as negative controls (Figure 6I and Figure S6F). Subsequent staining with streptavidin-fluorophores and FACS analysis revealed that even 30 s of irradiation induced significant *cis*-labeling in CD40L-Lantern cells (Figure S6G-H). Extended irradiation increased labeling efficiency from 43% to 62%, with a mean fluorescence intensity boost of approximately 2.2-fold (Figure S6G-H). For *trans*-labeling, CD40-expressing cells exhibited substantially higher labeling efficiency (up to 28.6-fold) compared to untransfected cells after 30 s of illumination (Figure 6J and Figure S6I-J). Together, these data demonstrate that Lantern can effectively report ligand-dependent cell-cell interactions.

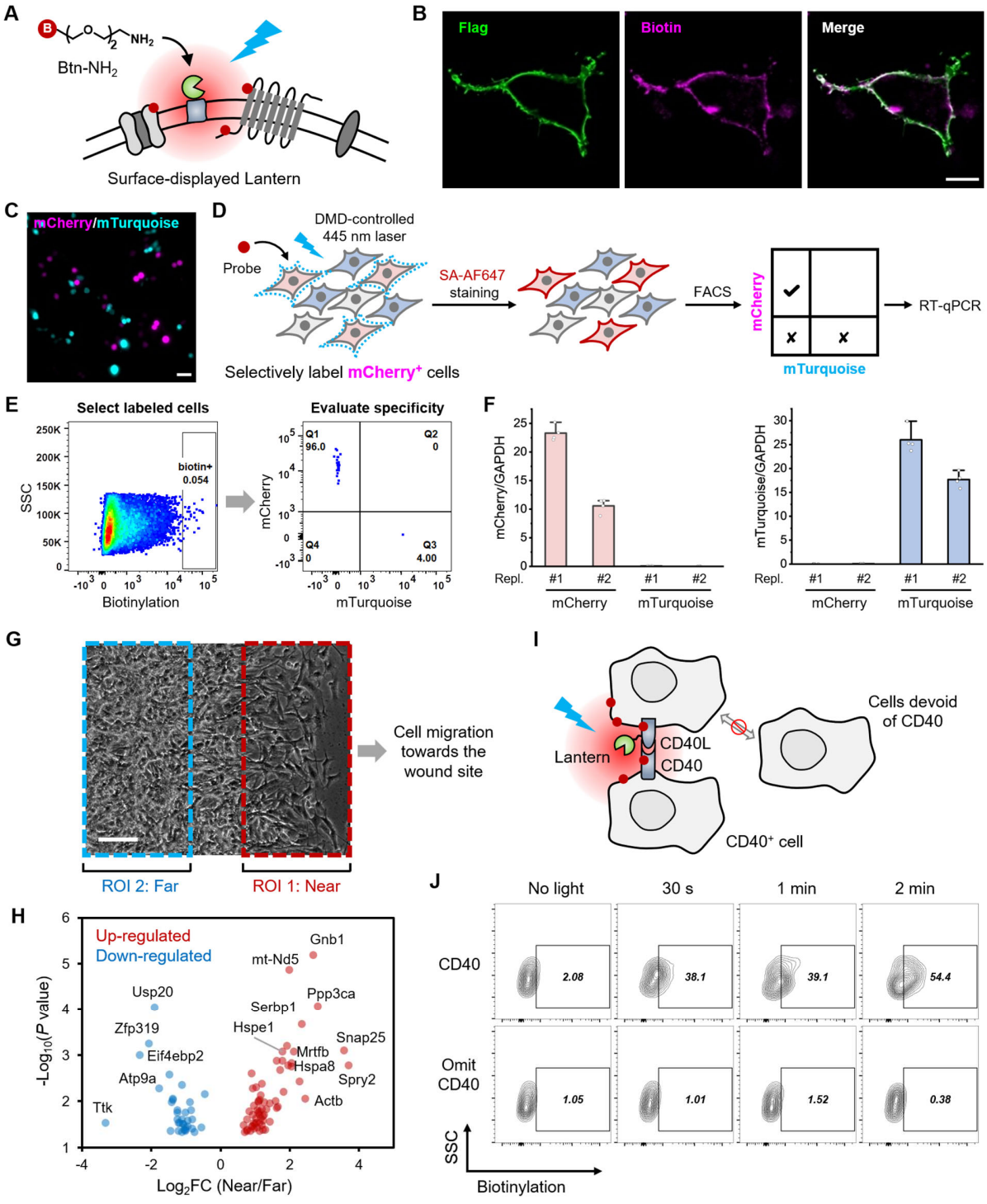


Figure 6. Spatially resolved cellular tagging with Lantern. (A) Schematic illustration of cell-surface labeling using Lantern-TM. **(B)** Representative immunofluorescence images of HEK293T cells labeled with Lantern-TM. Scale bar: 10 μm. **(C)** Fluorescence images of co-cultured HEK293T cells expressing either mCherry (magenta) or mTurquoise (cyan). Scale bar: 50 μm. **(D)** Schematic of DMD-controlled

cellular tagging and sorting from a mixed cell population. Cells expressing mCherry and Lantern-TM are selectively illuminated with a 445 nm laser in the presence of 2 mM Btn-NH_2. Biotinylated cells are subsequently enriched by flow cytometry and analyzed by RT-qPCR. **(E)** Representative flow cytometry plot demonstrating the selective enrichment of mCherry-expressing cells. **(F)** RT-qPCR analysis of normalized expression levels of *mCherry* (left) and *mTurquoise* (right) in sorted cells. Cells were selectively labeled based on mCherry (2 replicates) or mTurquoise (2 replicates) expression, with levels normalized to *GAPDH*. **(G)** Brightfield images of MC38 cells from a wound healing assay, captured after 24 h of migration. Scale bar: 100 μm. **(H)** Volcano plot showing differentially expressed genes in migrating cells. Red and blue dots indicate RNAs that are up-regulated and down-regulated, respectively, in cells closer to the wound site. **(I)** Schematic diagram illustrating CAP-CELL labeling for cell–cell interactions. **(J)** Flow cytometry plots depicting *trans*-labeling of cells expressing CD40 (top) versus control cells (bottom). The experiment was repeated three times.

Discussion

In this study, we engineered a genetically encoded photocatalyst, Lantern, via directed evolution. Previous work by Ogilby and co-workers produced miniSOG variants (SOPP, SOPP2, and SOPP3) using rational design to enhance singlet oxygen quantum yields and improve photocatalytic PL outcomes. However, large-scale screening of miniSOG variants, particularly for RNA labeling, has not been reported. Our approach was enabled by a novel selection platform that quantitatively measures intracellular RNA modifications in mammalian cells. Although phage and yeast display methods are common in directed evolution, mutants selected in microbial systems often underperform in the mammalian cytoplasm. Therefore, we directly evolved Lantern within the mammalian context by linking phenotype and genotype via an RNA self-labeling strategy. When tested, the selected mutants demonstrated robust activity in mammalian cells. In principle, this RNA self-labeling method can be readily extended to engineer other RNA-modifying enzymes.

Compared to earlier CAP-seq approaches using miniSOG, Lantern-mediated CAP-seq yielded significantly greater transcriptome coverage while maintaining high spatial specificity for profiling ERM-proximal RNAs. Similarly, Lantern-mediated CAP-MS achieved stronger protein labeling than methods such as RinID and LITag. Moreover, the high spatial resolution afforded by light allows Lantern to selectively tag cells through surface protein labeling, facilitating the study of specific cell types and their interacting partners in complex cultures or tissue samples. Additionally, Lantern-mediated PL dramatically improved labeling kinetics over conventional enzyme-mediated PL methods, which typically require 1 min (e.g., APEX2) or over 10 min (e.g., TurboID) for labeling. In contrast, Lantern-mediated photocatalytic reactions operate with as fast

as 1-s temporal precision, which is suitable for temporally resolved profiling of rapid biological processes such as the assembly of biomolecular complexes.

In our investigation of SG components during assembly, we observed that the SG transcriptome is enriched for RNAs with longer transcript lengths and higher levels of m^{6}A modifications, which is consistent with previous findings. Notably, we identified a subset of transcripts characterized by long coding sequences but low m^{6}A levels that bind to G3BP1 even before stress induction and maintain robust interactions during SG assembly. These “stress-independent” RNA interactors, comprising about 22% of all G3BP1-associated RNAs, differ from canonical SG and P-body components, suggesting that they may reflect the intrinsic organization of G3BP1 nanodomains within mature SG cores.

We also observed a minor fraction of ERM transcripts that interact with G3BP1 in a stress-dependent manner. Prior imaging studies have demonstrated that SGs can undergo fission at ER contact sites, implying frequent interactions between mature SGs and the ER membrane. Our immunofluorescence imaging revealed small clusters of G3BP1 associated with ER tubules as early as 10 min post-stress (Figure 3G). Collectively, these transcriptomic and imaging data indicate that SG-ER interactions are initiated early in the stress response. Recent studies further suggest that phospholipid enrichment within phase-separated protein condensates, combined with the hydrophobic nature of the ER membrane, may promote SG assembly under stress[38].

RNA m^{6}A modification is closely linked to cytoplasmic membraneless organelles such as SGs and P-bodies. Our proteomic analysis confirmed the enrichment of m^{6}A reader proteins, including YTHDF1-3, IGF2BP1-3, and FMR1, whereas the nuclear m^{6}A reader YTHDC was notably excluded from our dataset. Under stress, both m^{6}A RNAs and m^{6}A reader proteins exhibited a significant increase in enrichment ratio by G3BP1-Lantern. Temporally resolved analysis of enrichment revealed that the most pronounced changes for both RNA and protein components occurred between 5- and 30-min post-stress. Moreover, RNA levels rises more steeply than those of proteins during the initial 5-10 min. In summary, the integrated transcriptomic and proteomic analyses of our CAP-seq and CAP-MS datasets suggest a more rapid response of m^{6}A-modified RNAs than m^{6}A reader proteins during SG assembly.

Although Lantern-mediated photocatalytic PL exhibits rapid and efficient labeling capabilities, it currently requires high probe concentrations to effectively compete with endogenous nucleophiles such as water and glutathione. Future optimization should focus on developing probes with enhanced nucleophilicity or engineering flavoproteins capable of operating via a nucleophile-independent, photo-induced electron transfer mechanism.

Acknowledgments

This work was supported by the Ministry of Science and Technology (2022YFA1304700), the National Natural Science Foundation of China (32088101), and Beijing National Laboratory for Molecular Sciences (BNLMS-CXXM-202403). PZ is sponsored by Bayer Investigator Award. We thank the National Center for Protein Sciences at Peking University in Beijing, China, for assistance with Fragment Analyzer 12. The measurements of mass spectrometry were performed at the Analytical Instrumentation Center of Peking University. We thank the help from Dr. Wen Zhou at PKUAIC.

Author Contributions

Y.F., Z.R., F.Z., R.W., and P.Z. designed experiments; Y.F. performed directed evolution experiments and Lantern characterizations; Y.F., Z.R., F.Z. performed stress granule experiments; Y.F. and R.W. performed selective celllular tagging experiments; Y.F., Z.R., F.Z., R.W., and P.Z. analyzed data; Y.F. and P.Z. wrote the paper with inputs from all authors.

Declaration of Interests

The authors declare no competing interests.

References

1. Saxton, R.A. & Sabatini, D.M. mTOR Signaling in Growth, Metabolism, and Disease. *Cell* **168**, 960-976 (2017).
2. Kamel, W. et al. Alphavirus infection triggers selective cytoplasmic translocation of nuclear RBPs with moonlighting antiviral roles. *Molecular Cell* **84**, 4896-4911.e4897 (2024).
3. Safieddine, A. et al. Cell-cycle-dependent mRNA localization in P-bodies. *Molecular Cell* **84**, 4191-4208.e4197 (2024).
4. Wheeler, J.R., Matheny, T., Jain, S., Abrisch, R. & Parker, R. Distinct stages in stress granule assembly and disassembly. *eLife* **5** (2016).
5. Roux, K.J., Kim, D.I., Raida, M. & Burke, B. A promiscuous biotin ligase fusion protein identifies proximal and interacting proteins in mammalian cells. *Journal of Cell Biology* **196**, 801-810 (2012).
6. Branon, T.C. et al. Efficient proximity labeling in living cells and organisms with TurboID. *Nature Biotechnology* **36**, 880-887 (2018).
7. Martell, J.D. et al. Engineered ascorbate peroxidase as a genetically encoded reporter for electron microscopy. *Nature Biotechnology* **30**, 1143-1148 (2012).
8. Rhee, H.-W. et al. Proteomic Mapping of Mitochondria in Living Cells via Spatially Restricted

Enzymatic Tagging. *Science* **339**, 1328-1331 (2013).
9. Lam, S.S. et al. Directed evolution of APEX2 for electron microscopy and proximity labeling. *Nature Methods* **12**, 51-54 (2014).
10. Loh, K.H. et al. Proteomic Analysis of Unbounded Cellular Compartments: Synaptic Clefts. *Cell* **166**, 1295-1307.e1221 (2016).
11. Emara, M.M. et al. Hydrogen peroxide induces stress granule formation independent of eIF2 α phosphorylation. *Biochemical and Biophysical Research Communications* **423**, 763-769 (2012).
12. Fang, Y. & Zou, P. Photocatalytic Proximity Labeling for Profiling the Subcellular Organization of Biomolecules. *ChemBioChem* **24** (2023).
13. Geri, J.B. et al. Microenvironment mapping via Dexter energy transfer on immune cells. *Science* **367**, 1091-+ (2020).
14. Wang, P. et al. Mapping spatial transcriptome with light-activated proximity-dependent RNA labeling. *Nature Chemical Biology* **15**, 1110-1119 (2019).
15. Ding, T. et al. Chromophore‐Assisted Proximity Labeling of DNA Reveals Chromosomal Organization in Living Cells. *Angewandte Chemie International Edition* **59**, 22933-22937 (2020).
16. Zheng, F., Yu, C., Zhou, X. & Zou, P. Genetically encoded photocatalytic protein labeling enables spatially-resolved profiling of intracellular proteome. *Nature Communications* **14** (2023).
17. McIntosh, J.R. et al. A Genetically Encoded Tag for Correlated Light and Electron Microscopy of Intact Cells, Tissues, and Organisms. *PLoS Biology* **9** (2011).
18. Zhai, Y. et al. Spatiotemporal-resolved protein networks profiling with photoactivation dependent proximity labeling. *Nature Communications* **13** (2022).
19. Ren, Z., Tang, W., Peng, L. & Zou, P. Profiling stress-triggered RNA condensation with photocatalytic proximity labeling. *Nature Communications* **14** (2023).
20. Hananya, N., Ye, X., Koren, S. & Muir, Tom W. A genetically encoded photoproximity labeling approach for mapping protein territories. *Proceedings of the National Academy of Sciences* **120** (2023).
21. Grünwald, D. & Singer, R.H. In vivo imaging of labelled endogenous β-actin mRNA during nucleocytoplasmic transport. *Nature* **467**, 604-607 (2010).
22. Lin, C., Liu, L. & Zou, P. Functional imaging-guided cell selection for evolving genetically encoded fluorescent indicators. *Cell Reports Methods* **3** (2023).
23. Matreyek, K.A., Stephany, J.J., Chiasson, M.A., Hasle, N. & Fowler, D.M. An improved platform for functional assessment of large protein libraries in mammalian cells. *Nucleic Acids Research* (2019).
24. Swartz, T.E. et al. The Photocycle of a Flavin-binding Domain of the Blue Light Photoreceptor Phototropin. *Journal of Biological Chemistry* **276**, 36493-36500 (2001).
25. Torra, J. et al. Tailing miniSOG: structural bases of the complex photophysics of a flavin-

binding singlet oxygen photosensitizing protein. *Scientific Reports* **9** (2019).
26. Dietler, J. et al. Signal transduction in light-oxygen-voltage receptors lacking the active-site glutamine. *Nature Communications* **13** (2022).
27. Westberg, M., Bregnhøj, M., Etzerodt, M. & Ogilby, P.R. No Photon Wasted: An Efficient and Selective Singlet Oxygen Photosensitizing Protein. *The Journal of Physical Chemistry B* **121**, 9366-9371 (2017).
28. Gollmer, A. et al. Singlet Oxygen Sensor Green®: Photochemical Behavior in Solution and in a Mammalian Cell. *Photochemistry and Photobiology* **87**, 671-679 (2011).
29. Fazal, F.M. et al. Atlas of Subcellular RNA Localization Revealed by APEX-Seq. *Cell* **178**, 473-490.e426 (2019).
30. Reid, D.W. & Nicchitta, C.V. Diversity and selectivity in mRNA translation on the endoplasmic reticulum. *Nature Reviews Molecular Cell Biology* **16**, 221-231 (2015).
31. Mavylutov, T., Chen, X., Guo, L. & Yang, J. APEX2- tagging of Sigma 1-receptor indicates subcellular protein topology with cytosolic N-terminus and ER luminal C-terminus. *Protein & Cell* **9**, 733-737 (2017).
32. Padrón, A., Iwasaki, S. & Ingolia, N.T. Proximity RNA Labeling by APEX-Seq Reveals the Organization of Translation Initiation Complexes and Repressive RNA Granules. *Molecular Cell* **75**, 875-887.e875 (2019).
33. Xiao, Y. et al. Profiling of RNA-binding protein binding sites by in situ reverse transcription-based sequencing. *Nature Methods* **21**, 247-258 (2024).
34. Huang, H. et al. Recognition of RNA N^6-methyladenosine by IGF2BP proteins enhances mRNA stability and translation. *Nat Cell Biol* **20**, 285-295 (2018).
35. Ries, R.J. et al. m^6A enhances the phase separation potential of mRNA. *Nature* **571**, 424-428 (2019).
36. Fu, Y. & Zhuang, X. m^6A-binding YTHDF proteins promote stress granule formation. *Nat Chem Biol* **16**, 955-963 (2020).
37. Edupuganti, R.R. et al. N^6-methyladenosine (m^6A) recruits and repels proteins to regulate mRNA homeostasis. *Nature Structural & Molecular Biology* **24**, 870-878 (2017).
38. Dumelie, J.G. et al. Biomolecular condensates create phospholipid-enriched microenvironments. *Nature Chemical Biology* **20**, 302-313 (2023).

Supplementary Files

This is a list of supplementary files associated with this preprint. Click to download.

- SIv5.3250529.pdf
- Supplementarytables.rar